Molybdenum Based 2D Conductive Metal–Organic Frameworks as Efficient Single-atom Electrocatalysts for N_2 Reduction: A Density Functional Theory Study

Yongxiu Sun[1], Wenwu Shi[2], Mengxuan Sun[1], Qisheng Fang[1], Xiaohe Ren[1], Yijun Yan[1], Ziwei Gan[1], Yong-Qing Fu[3], Ahmed Elmarakbi[3], Zhijie Li*[,1], Zhiguo Wang*[,2]

1. *School of Physics, University of Electronic Science and Technology of China, Chengdu, 610054, P.R. China*
2. *School of Information and Software Engineering, University of Electronic Science and Technology of China, Chengdu, 610054, P.R. China*
3. *Faculty of Engineering and Environment, Northumbria University, Newcastle Upon Tyne, NE1 8ST, UK*

*Correspondence authors. E-mail: zgwang@uestc.edu.cn (Z. Wang);

zhijieli@uestc.edu.cn (Z. Li).

Abstract:

Electrocatalytic nitrogen reduction reaction (NRR) is a sustainable and eco-friendly process to generate ammonia (NH_3). However, there are significant challenges including low catalytic performance, instability, and poor selectivity, which hinder its rapid development. Herein, a series of two-dimensional (2D) conductive metal-organic frameworks (i.e., $TM_3(HHTT)_2$, TM = Sc, Ti, V, Cr, Mo, W, Mn, Fe, Co, Ni, Cu and Zn) are investigated as single atom catalysts (SACs) for NRR process by the density functional theory (DFT). The obtained results of Gibbs free energies of adsorption for N_2, *NNH, *NH_3, which are commonly used as activity descriptors to screen the effectiveness of catalysts, show that the $Mo_3(HHTT)_2$ monolayer (among all the $TM_3(HHTT)_2$ ones) can activate N≡N bonds, stabilize the adsorbed *NNH, and achieve the desorption of NH_3. The $Mo_3(HHTT)_2$ monolayer also exhibits an excellent structural stability (with values of E_f = -2.96 eV and U_{diss} = 1.28 V). N_2 can be effectively reduced into NH_3 on the $Mo_3(HHTT)_2$ monolayer with a low limiting

potential of -0.60 V along the distal pathway. Furthermore, the σ-donation and π* back-donation of N_2 adsorbed onto the $Mo_3(HHTT)_2$ monolayer indicates an excellent electrical conductivity of $Mo_3(HHTT)_2$, which is beneficial for the effective electron transfer during the NRR process. Furthermore, the $Mo_3(HHTT)_2$ monolayer exhibits considerable selectivity for the NRR process over the hydrogen evolution reaction. Our study proved that this 2D c-MOFs carrying TM of the $Mo_3(HHTT)_2$ monolayer can be used as a promising catalyst for nitrogen fixation.

Keywords: single-atom catalysts; metal-organic frameworks; density functional theory; nitrogen reduction reaction

1. Introduction

Ammonia (NH_3) is not only an essential primary raw material for producing various industrial chemicals such as fertilizers, but also a stable carrier of hydrogen production [1-3]. Due to the robust dipole moment of N_2 and ultra-high bond energy of triple N≡N (940.95 kJ mol^{-1}), NH_3 is dominantly synthesized using the technology of conventional Haber-Bosch based on a dissociation reaction involving co-activation of atmospheric nitrogen under high pressure (100-200 atm) and temperature (573-773 K), using high purity gases of N_2 and H_2 [4-7]. Due to the intensive use of fossil fuels, this Haber-Bosch process is a primary source of significant greenhouse gas emissions [8]. Therefore, it is crucial to explore alternative, effective and sustainable approaches to produce NH_3 via N_2 fixation under much milder process conditions [9].

Inspired by biological N_2 fixation, electrocatalytic nitrogen reduction reaction (NRR) is a prospective sustainable approach for the synthesis of NH_3, because this process can conduct at atmospheric pressure and room temperature, and utilizes water (H_2O) as the hydrogen resource [10, 11]. However, there are considerable challenges because its electrocatalysts have critical issues, such as poor catalytic activities and low selectivity,

mainly caused by the slow kinetics of reactions and the strong competitive reaction of hydrogen evolution reaction (HER) [11-13]. Therefore, the design and fabrication of highly efficient and selective NRR electrocatalysts are critically needed.

In recent years, numerous studies of the NRR electrocatalysts have been reported [14-21]. Electrocatalysts based on noble metals such as gold, ruthenium, and rhodium show high selectivity and good catalytic performance for the process of NRR [22-24]. However, they have significant issues of poor stability and high cost. To tackle this issue, embedding single transition metal (TM) atoms into 2D substrates have been widely explored as effective electrocatalysts for N_2 reduction [25-29]. Owing to their tunable electronic structures and low coordinated configurations, these single-atom catalysts (SACs) are developed to improve the electrocatalytic performance and selectivity of catalysts for the NRR process [30-34]. However, due to the d orbitals interactions in TMs, the TM atoms easily become severely agglomerated during the NRR process. Thus there is a critical need to find the appropriate methods to prevent the severe agglomeration of these TM atoms and boost their catalytic activities.

In numerous studies, graphene is widely used as a support for SACs [35, 36]. However, creating suitable holes in a two-dimensional (2D) planes while firmly embedding isolated metal atoms is difficult in large-scale application. 2D metal-organic frameworks (MOFs) have larger porosity, which facilitates the diffusion of gases, disperses the active metal ions uniformly on the plane [37] and greatly increases the catalytic sites. Self-assembly of TM atoms with conjugated organic ligands containing functional groups can effectively form 2D conductive MOFs [38, 39]. Their effective coordination sites can stably and uniformly anchor single metal atoms and prevent their agglomeration. Therefore, these 2D c-MOFs can be applied as an ideal platform for immobilizing transition metal atoms. The charge redistribution and strong in-plane d-p conjugations can be generated by the TM atoms in these 2D c-MOFs, which could effectively facilitate the NRR process [40]. In addition, the 2D c-MOFs have ultrathin

thicknesses, large specific surface areas, abundant unsaturated active sites, large porosity, and tunable surface properties, all of which are beneficial to the electrocatalytic N_2 reduction reactions [41].

Previously, Xu et al. reported to use 2D MOFs of MC_4S_4 (M = Fe, Ru, Os, Co, Rh, Ir, Ni, Pd, Pt, Cr, Mn, Mo, and W) for the NRR process, and their results showed that OsC_4S_4 and RuC_4S_4 monolayers exhibit suitable NRR catalytic activities [42]. Li et al. systematically investigated the potential of coronene-based TM-perthiolated coronene as SACs for NRR, and their results showed that the N_2 molecules could be readily reduced to NH_3 on V/Fe-PTC [43]. Feng et al. proposed a 2D MOFs of $TM_3(C_2O)_{12}$, and reported that the $Mo_3(C_2O)_{12}$ monolayer exhibited an excellent electrocatalytic performance [44]. Zhang et al. investigated the possibilities of using Mo-based 2D $TM_3(C_6X_6)_2$, namely, $Mo_3(C_6X_6)_2$, as the electrocatalysts for NRR [45]. Lv et al. investigated a series of nitrogen-free MOFs of TM–benzenehexathiol (TM–BHT) for NRR and reported that Mo–BHT exhibited the suitable value of the U_L for the NRR [46]. It is noteworthy to mention that the conductivity of 2D MOFs determines the catalytic performance. Therefore, these 2D MOFs with their higher electrical conductivities are particularly suitable in the design of NRR electrocatalysts.

Recently, to obtain stable and conductive 2D MOFs, crystalline structures of electrically conducting $TM_3(HHTT)_2$ monolayers were formed by combining TM (Co and Ni) atoms with the ligand of 2,3,7,8,12,13-hexahydroxy tetraazanaphthotetraphene (HHTT) [47]. The energetic overlap of orbitals of the delocalization of the electronic charge in the conjugated structures and metal atoms could improve electrical conductivity of 2D MOFs [40]. Electronic structure, metal conductivity, and thermal stability of 2D c-MOFs can be restructured via applying the central bridging metal atoms [18]. For example, it was reported that the diameter of hexagonal mesoporous of 2D MOFs of $Cu_3(HHTT)_2$ is around 2.47 nm [36], which is essential for the gas-phase catalysis process and desorption of gas molecules. The $Cu_3(HHTT)_2$ MOF materials

were also reported to show good catalytic properties for CO_2 reduction reaction [37]. Recently, $Co_3(HHTT)_2$ monolayer was also reported as the oxygen reduction reaction (ORR) electrocatalyst [48].

Despite the above mentioned studies using the $TM_3(HHTT)_2$ catalysts for CO_2RR and ORR processes, there are few reports on the studies of mechanisms of using $TM_3(HHTT)_2$ electrocatalysts for the NRR process. In this study, the electrocatalytic performance of $TM_3(HHTT)_2$ (TM = Sc, Ti, V, Cr, Mo, W, Mn, Fe, Co, Ni, Cu and Zn) monolayers for the synthesis of NH_3 is studied by density functional theory (DFT). The obtained results suggest that among all $TM_3(HHTT)_2$, $Mo_3(HHTT)_2$ monolayer exhibits the best electrocatalytic performance on N_2 reduction due to its excellent performance in activating N_2, adsorption of *NNH intermediates, and desorption of NH_3. Moreover, it exhibits an excellent structural stability (e.g., E_f = -2.96 eV, and U_{diss} = 1.28 V), high catalytic activity (U_L = -0.60 V) and a good selectivity (U_d = -0.38 V) for the NRR. Our results show that the $Mo_3(HHTT)_2$ monolayer can be used as a promising electrocatalyst for NH_3 production from the gas of N_2.

2. Computational Details

The Vienna Ab initio Simulation Package (VASP) code was used to calculate the structure relaxation and total energy [49]. The Perdew–Burke–Ernzerhof (PBE) exchange-correlation functional with a generalized gradient approximation (GGA) was adopted to calculate the exchange-correlation potential. The ion-electron interaction was calculated by the projector augmented wave (PAW) pseudopotential, and the cutoff energy was set to 500 eV. The generalized gradient approximation of the Perdew-Burke-Ernzerhof (GGA-PBE) functional was used to calculate the exchange-correlation potential [50-52]. The van der Waals (vdW) correction described by the DFT-D3 was applied. [53]. The supercell contained a vacuum layer of 15 Å to avoid the interactions between two slabs, which is verified by the convergence of different vacuum layers. The convergence criterion of the force was set to 0.02 eV/Å. The Brillouin zone was

sampled with 3 × 3 × 1 Monkhorst-Pack mesh k-points [54]. The values of different K-points are checked and the results show that the K-points mesh with 3 × 3 × 1 is sufficient to achieve computational accuracy. The electronic properties were processed by the VASPKIT [55].

The Gibbs free energy (ΔG) was calculated based on the computational hydrogen electrode (CHE) model in the NRR performance [56].The value of ΔG for a proton-electron pair is 0.5 G(H_2, g) [57]. The change in the values of ΔG is defined as:

$$\Delta G = \Delta E + \Delta ZPE - T\Delta S + eU + \Delta G_{pH}, \qquad (1)$$

where ΔE denotes the reaction energy difference of intermediates, ΔZPE represents the change of the zero-point energy, and ΔS is the entropy change at the temperature of T= 298.15 K, both of which can be obtained from the vibrational frequency calculation. The entropy correction and zero-point energy of the gas phase molecules (H_2, N_2, and NH_3) are available from the NIST database [58], as listed in Table S1. The symbol e indicates the electrons transferred number, while symbol U indicates the applied electrode potential. Moreover, ΔG_{pH} is the pH-dependent free energy correction defined as $\Delta G_{pH} = 2.303 \times k_B T \times pH$, where k_B is the Boltzmann constant.

The limiting overpotential (U_L) has been calculated according to the equation:

$$U_L = -\Delta G_{max} / e, \qquad (2)$$

where ΔG_{max} is the maximum change of the Gibbs energy during the NRR process. The formation energy (E_f) per metal atom of the unit-cell $TM_3(HHTT)_2$ monolayers and dissolution potential (U_{diss}) are calculated using:

$$E_f = (E_{TM3(HHTT)2} - 3E_{TM} - 2E_{HHTT}) / 3, \qquad (3)$$

$$U_{diss} = U°_{diss}\,(\text{metal, bulk}) - E_f / ne, \qquad (4)$$

where $E_{TM3(HHTT)2}$, E_{TM}, and E_{HHTT} are the total energies of (1) the $TM_3(HHTT)_2$, (2) metal atom in bulk structure, and (3) HHTT organic ligands. The $U°_{diss}$ (metal, bulk)

denoted the standard dissolution potential of a bulk metal. The symbol n denotes the number of electrons in the dissolution [59]. Based on previous studies [60], when E_f < 0 eV, the $TM_3(HHTT)_2$ monolayer is considered as thermodynamically stable; when U_{diss} > 0 V, the $TM_3(HHTT)_2$ monolayer is considered as electrochemically stable. Table S2 lists the detailed data of E_f and U_{diss}.

3. Results and discussion

3.1 Anlaysis of Stability and Structure.

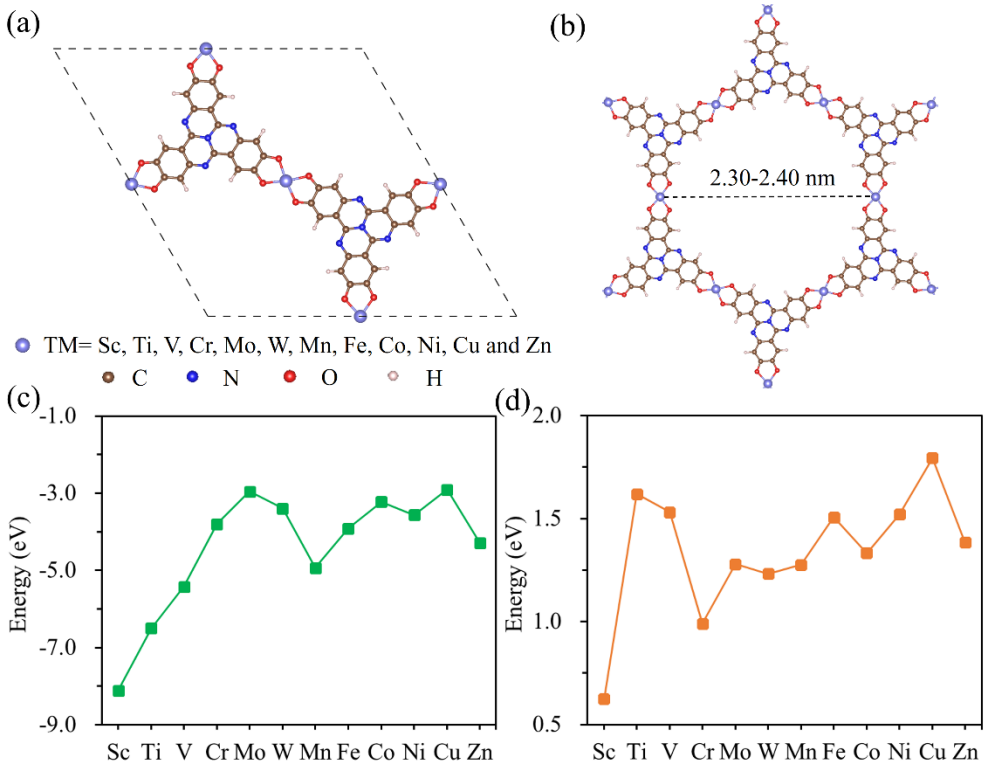

Figure 1. (a) Top view of pristine $TM_3(HHTT)_2$ monolayers. The atoms of TM, C, N, O, and H are described by purple, brown, blue, red, and white balls. (b) The metal macrocycles of $TM_3(HHTT)_2$ monolayers. (c)The E_f and (d) U_{diss} of unit cell of the $TM_3(HHTT)_2$ monolayers.

Before screening the NRR electrocatalytic properties of different $TM_3(HHTT)_2$ monolayers, the optimized structures of $TM_3(HHTT)_2$ monolayers were theoretically

investigated by using DFT calculations. The obtained results are shown in Fig. 1(a). For all the different optimized structures, all the atoms are located in the same plane without bending, meaning that these two-dimensional structures can co-exist stably. The detailed optimized lattice parameters of $TM_3(HHTT)_2$ are listed in Table S2.

Honeycomb-like 2D nets are formed by the coordination of the TM and triangular HHTT ligands, as shown in Fig.1(b). Each HHTT ligand, as the coordination organic linker, is attached to three equivalent transition metal atoms. The transition metal and the surrounding O_4 atoms form the plane and conductive structure, which effectively prevents the formation of metal clusters and improves the utilization of transition metal atoms. The pore size of the honeycomb-like 2D structure of the $TM_3(HHTT)_2$ is as large as 2.30 ~ 2.40 nm. The large pore size structure can facilitate the transport of N_2 and NH_3 gases.

The thermodynamic and electrochemical stabilities of $TM_3(HHTT)_2$ monolayers were further investigated. The values of E_f and U_{diss} of $TM_3(HHTT)_2$ monolayers were calculated to avoid the diffusion and aggregation of TM atoms during the NRR process. The results are shown in Figs. 1(c) and 1(d), respectively. The values of E_f for the $TM_3(HHTT)_2$ monolayers are all less than 0. For the calculated U_{diss} values of the $TM_3(HHTT)_2$ monolayers, all the values are much higher than 0. The results indicate that these $TM_3(HHTT)_2$ all have good stability and should be easily experimentally synthesized. According to the calculated results, all the twelve $TM_3(HHTT)_2$ monolayers we have studied have good thermodynamic and electrochemical stabilities for NNR catalytic applications.

3.2. Screening the $TM_3(HHTT)_2$ for NRR catalysis.

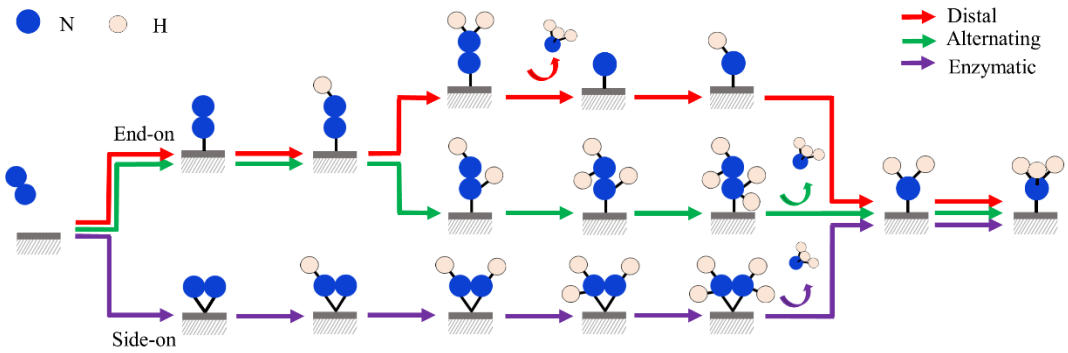

Figure 2. Schematic representation of NRR process along distal, alternating, and enzymatic pathways.

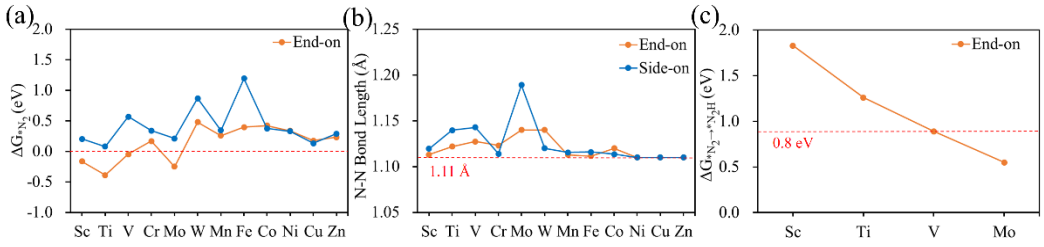

Figure 3. (a) The values of ΔG^*_{N2} for N_2 on $TM_3(HHTT)_2$ monolayers in end-on and side-on configurations. (b) The N−N bond lengths of N_2-$TM_3(HHTT)_2$ in end-on and side-on configurations. (c) The values of $\Delta G_{*N2\rightarrow *N2H}$ for $Mo_3(HHTT)_2$ monolayer.

Fig. 2 displays three typical reaction mechanisms involved in the NRR process, e.g., distal, alternating, and enzymatic pathways. For N_2 adsorption on the $TM_3(HHTT)_2$ monolayer, there are two types of configurations, i.e., end-on and side-on. Only one N atom is bound to the Mo atom of the $TM_3(HHTT)_2$ monolayer for the end-on configuration. In contrast, both atoms of the N_2 gas molecules form the bonding of Mo-N with the $TM_3(HHTT)_2$ monolayer for the side-on configuration. With these two configurations, six consecutive protonation processes for the NRR follows the process: N_2 (g) + $6H^+$ + $6e^-$ → $2NH_3$. The NRR process will be along a distal mechanism, or following an alternating mechanism for N_2 adsored on the $TM_3(HHTT)_2$ monolayer in the end-on configuration. The enzymatic mechanism will occur along the side-on configuration [61].

The electrocatalytic performance of $TM_3(HHTT)_2$ monolayers for the NRR were screened based on the following three criteria: (1) The catalyst can effectively activate N≡N bond and can form N_2 molecules chemisorption (e.g., $\Delta G^*_{N2} < 0$); (2) The hydrogenation of the $*N_2$ to $*N_2H$ has a small value of Gibbs free energy change, which can accelerate the NRR process (e.g., $\Delta G_{*N2 \rightarrow *N2H} < 0.80$ eV); (3) The intermediate of $*NH_3$ with smaller Gibbs free energy change can easily dispel from the surface of the catalyst (e.g., $\Delta G_{*NH2 \rightarrow *NH3} < 0.80$ eV). If all the above three screening criteria can be met, the candidate electrocatalytic monolayers could serve as suitable NRR catalysts with rapid desorption capability of NH_3, stable generation of intermediates, and low limiting potentials.

A prerequisite for the NRR process is that N_2 molecules can be spontaneously adsorbed on the $Mo_3(HHTT)_2$ monolayer. The N≡N triple bonds were weakened. The corresponding values of Gibbs free energy change for N_2 adsorption on the $TM_3(HHTT)_2$ monolayers for the end-on configuration and side-on configuration were studied as shown in Fig. 3(a). All detailed results of ΔG_{*N2} are listed in Table S3. If $\Delta G_{*N2} < 0$ eV, this indicates a strong N_2 adsorption ability of the electrocatalysts. The values of ΔG^*_{N2} for all the $TM_3(HHTT)_2$ monolayers in the side-on configuration are positive, which indicates that it is inactive for N_2 absorption. Thus, N_2 adsorption on these $TM_3(HHTT)_2$ monolayers in side-on configurations is unsuitable for the subsequent NRR process and excluded from the following studies. Whereas for N_2 adsorption cases on $Sc_3(HHTT)_2$, $Ti_3(HHTT)_2$, $V_3(HHTT)_2$, and $Mo_3(HHTT)_2$ monolayers in their end-on configurations, the values of ΔG_{*N2} are negative, indicating that these four types of 2D c-MOFs can effectively adsorb and activate N_2 molecules. Thus, the $Sc_3(HHTT)_2$, $Ti_3(HHTT)_2$, $V_3(HHTT)_2$, and $Mo_3(HHTT)_2$ monolayers have been selected for the further screening studies.

It should be noted that the bond length of N-N after adsorption is a direct indicator for the degree of activations. The N atom becomes readily bound to the proton-electron pairs after the N-N length is stretched. Contrast with the N-N bond length of the N_2 gas

molecules (1.11Å), these N_2 adsorptions on $TM_3(HHTT)_2$ monolayers are stretched into different degrees, which is different for the end-on configuration and side-on configuration as shown in Fig. 3(b). For the end-on configuration, the lengths of N-N bond of N_2 are elongated to 1.12 Å ($Sc_3(HHTT)_2$), 1.13 Å ($Ti_3(HHTT)_2$), 1.12 Å ($V_3(HHTT)_2$), and 1.14 Å ($Mo_3(HHTT)_2$) from 1.11 Å for the isolated N_2 molecules.

Based on the previous studies [61, 62], the protonation step of $*N_2$ to *NNH or $*NH_2$ to $*NH_3$ is the decisive step in the NRR process. Therefore, most transition-metal-based catalysts exhibit an essential hydrogenation step in a maximum positive value of ΔG along different catalytic pathways. The values of the $\Delta G_{*N2\rightarrow*NNH}$ for the $Sc_3(HHTT)_2$, $Ti_3(HHTT)_2$, $V_3(HHTT)_2$, and $Mo_3(HHTT)_2$ monolayers were investagied as shown in Fig. 3(c). The $\Delta G_{*N2\rightarrow*N2H}$ of $Sc_3(HHTT)_2$, $Ti_3(HHTT)_2$, and $V_3(HHTT)_2$ monolayers are 1.83, 1.26, and 0.89 eV, which cannot meet the second screening criteria ($\Delta G_{*N2\rightarrow*N2H} < 0.80$ eV). The above results indicate that the hydrogenation of $*N_2$ to $*N_2H$ cannot be achieved on the $Sc_3(HHTT)_2$, $Ti_3(HHTT)_2$, and $V_3(HHTT)_2$ monolayers. Whereas the $\Delta G_{*N2\rightarrow*N2H}$ for $Mo_3(HHTT)_2$ monolayer is 0.55 eV, which has met the requirement of the second screening criteria. Therefore, the $Mo_3(HHTT)_2$ monolayer will be selected for the third screening step. The obtained value of $\Delta G_{*NH2\rightarrow*NH3}$ for the $Mo_3(HHTT)_2$ monolayer is 0.60 eV. The above results indicate that the $Mo_3(HHTT)_2$ monolayer may be a suitable electrocatalyst for the NRR process.

3.3. Full Reaction Pathways on $Mo_3(HHTT)_2$

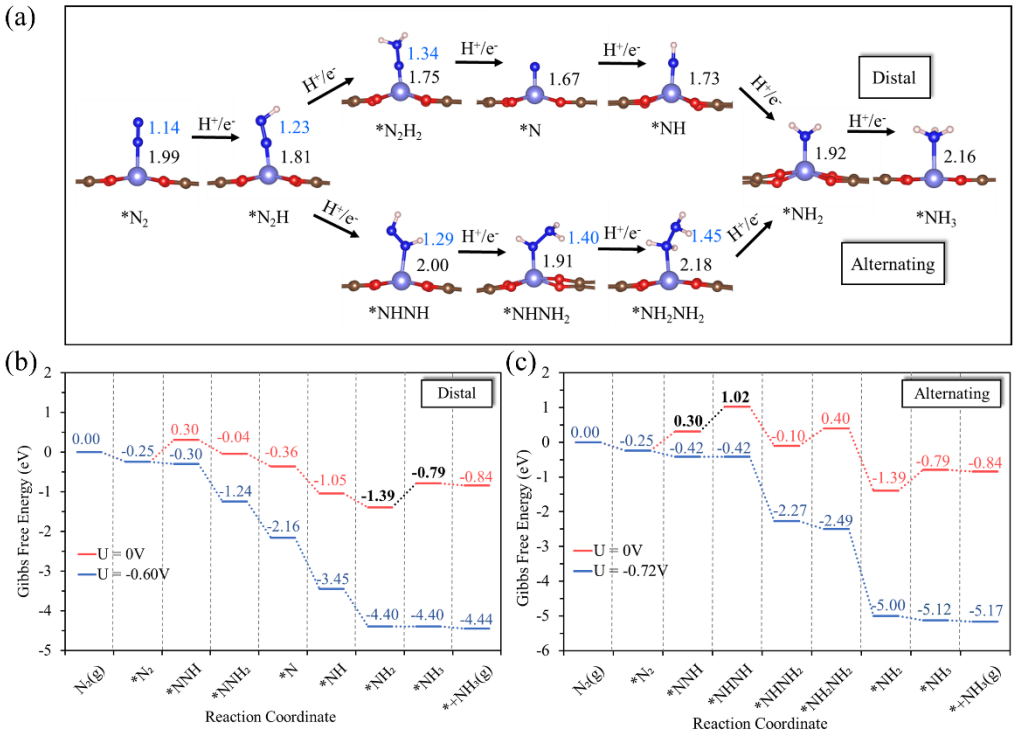

Figure 4. (a) Side views of the optimized structure of the intermediates along distal and alternating pathways for the NRR process. The N–N and Mo–N bond (Å) are shown in blue and black font, respectively. Here * represents the intermediates species. Gibbs free energy diagrams on the surface of the $Mo_3(HHTT)_2$ monolayer for the NRR at zero and respective onset potentials along the (b) distal and (c) alternating pathways.

The N_2 adsorption onto the $Mo_3(HHTT)_2$ monolayer in the end-on configuration can be efficiently activated. We have further studied the corresponding optimized structure of the intermediates as shown in Fig. 4(a). The obtained values of the Gibbs free energy on the surface of the $Mo_3(HHTT)_2$ monolayer for the NRR process along distal pathway, and along an alternating pathway are shown in Figs. 4(b) and 4(c), respectively. All the corresponding details of parameters are listed in Table S4. For the distal pathway, the N atom, which is not bounded to the Mo atom, has been reacting with the proton-electron pairs. While, for the alternating pathway, the both two N atoms are attacked by the proton-electron pairs [63]. These two pathways generate an NH_3 molecule involving six proton-electron pairs transfer processes. The value of the Gibbs free energy for N_2

adsorption on the $Mo_3(HHTT)_2$ monolayer is 0.21 eV in the side-on configuration, indicating that N_2 cannot be activated on the surface of the $Mo_3(HHTT)_2$ monolayer. Thus, its enzymatic mechanism is not considered.

The Gibbs free energy of N_2 atoms adsorption on the site of Mo atom of the $Mo_3(HHTT)_2$ monolayer is -0.25 eV along the distal pathway for NRR. Moreover, the N-N length is enlarged to 1.14 Å from 1.11 Å. In this process, the reaction of $*N_2 + (H^+ / e^-) \rightarrow *NNH$ is the first step of hydrogenation with a Gibbs free energy of 0.30 eV with the N-N length of 1.23 Å. The N-N bond length of intermediate of $*NNH_2$ with the Gibbs free energy of -0.04 eV is further elongated to 1.34 Å. All the results indicate that the activated degree of the N_2 molecule continues to increase. When the proton-electron pairs are bonded to the distal N of $*NNH_2$ intermediate on the surface of the $Mo_3(HHTT)_2$ monolayer, the first NH_3 is generated. Then, there is only one N atom at the Mo site on the surface of the $Mo_3(HHTT)_2$ monolayer. The value of the Gibbs free energy for the intermediate of *N is decreased to -0.36 eV. The proton-electron pairs attack the N atom of the intermediate of *N until the second NH_3 molecule is produced. The values of the ΔG for the processes of the $*N \rightarrow *NH$ and $*NH \rightarrow *NH_2$ are -0.69 eV and -0.34 eV. For the last step of hydrogenation, the $\Delta G_{*NH2 \rightarrow *NH3}$ is 0.60 eV, which is a potential-determining step (PDS) for the NRR on the $Mo_3(HHTT)_2$ monolayer along the distal pathway. Thus, the limiting potential of the $Mo_3(HHTT)_2$ monolayer is -0.60 V, which is more suitable for the NRR catalytic process if compared to the value of the Ru(0001) with the limiting potential of -0.98 V [64].

The first two and last two steps of the alternating pathway on the surface of the $Mo_3(HHTT)_2$ monolayer are the same as those of the distal pathway. The process of $*NHNH \rightarrow *NHNH_2$ with the ΔG of 0.72 V is the PDS for the alternating pathway. The values of free energy of $*NHNH_2$ and $*NH_2NH_2$ are -0.10 eV and 0.40 eV, respectively. The first NH_3 molecule is produced after the H^+/e^- pair attacks the intermediate of $*NHNH_2$. The following hydrogenation process produces the second NH_3 molecule. The NRR process can spontaneously occur with the applied electrode

potentials of −0.60 and −0.72 V along distal and alternating pathways. The values of U_L for the $Mo_3(HHTT)_2$ monolayer along the distal and alternating pathways are more significant than those for the reported Ru(0001) (−0.98 V) [64, 65]. Moreover, the summary of the NRR electrocatalytic performance with the reported electrocatalysts, including reaction pathways, potential-determining step (PDS) and limiting overpotential (U_L) is listed in Table S7. The above results show that the $Mo_3(HHTT)_2$ monolayer should have a good NRR catalytic performance.

3.4 NRR Catalytic Mechanisms.

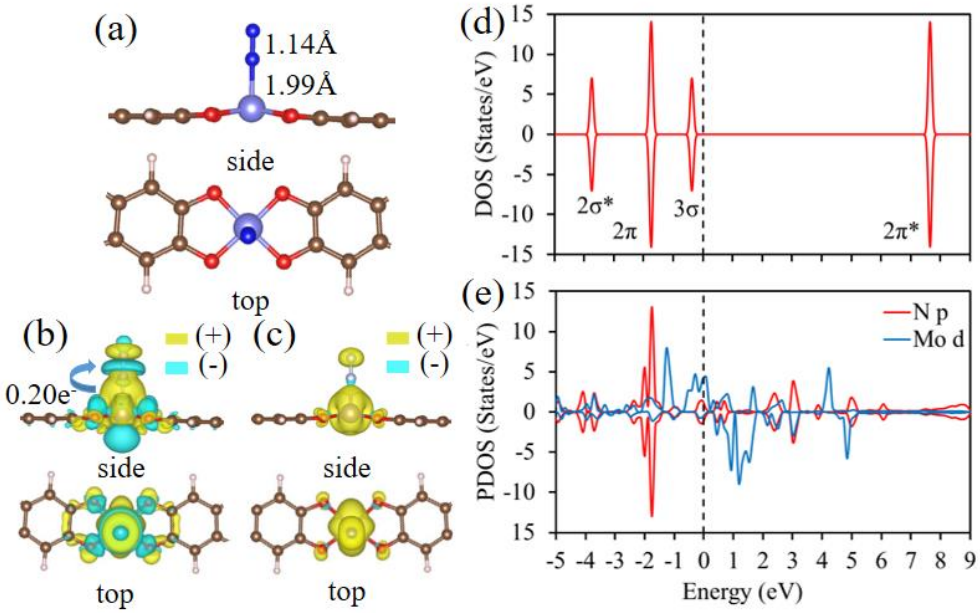

Figure 5. Side and top views of (a) optimized structure, (b) charge density difference, and (c) spin density of N_2 adsorbed on $Mo_3(HHTT)_2$ monolayer. The yellow regions indicate the accumulation of charge or spin density, and the blue regions indicate the depletion of charge or spin density. The isosurface level is set to 0.002 e/Å^3. PDOS of (d) free N_2 and (e) N_2 adsorbed on $Mo_3(HHTT)_2$ monolayer.

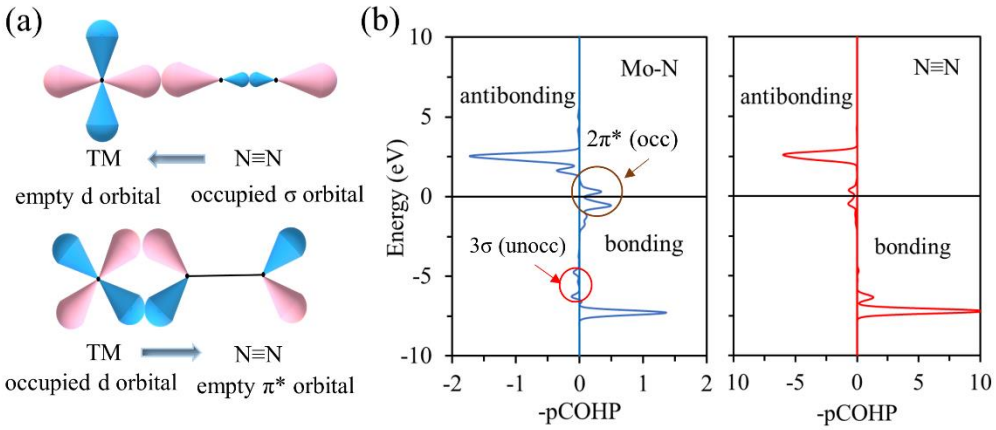

Figure 6. (a) Schematic diagram for the electron orbitals of N_2 adsorption on $Mo_3(HHTT)_2$ monolayer. (b) The -pCOHP for the Mo−N and N≡N bonds of the N_2 adsorption on $Mo_3(HHTT)_2$ monolayer.

To understand the cooperativity between the Mo atoms and the organic ligands in the NRR process, the electron localization function (ELF) of the $Mo_3(HHTT)_2$ monolayer was calculated as shown in Fig. S1 (a). The values of ELF > 0.5 demonstrate the covalent characteristics of the C−C, C−N, C−H, and C−O bonds, which indicates that electrons of HHTT are localized. The electrons of the O atoms in the $Mo_3(HHTT)_2$ monolayer are in the localized state, which facilitates the anchoring of lone-pair electrons to Mo atoms. The above results indicate that the Mo and O atoms could act as the active center of the $Mo_3(HHTT)_2$ monolayer for the NRR process. Therefore, the catalytic performance for NRR of the $Mo_3(HHTT)_2$ monolayer can be achieved via the synergistic effect between the Mo atoms and organic ligands of HHTT. The total magnetic moment of the $Mo_3(HHTT)_2$ monolayer is 6.94 μB. The NRR catalytic process can be facilitated by the highly spin-polarized transition-metal atoms [66-68]. The spin density diagram is illustrated in Fig. S1(c). The central magnetic regions are located around Mo atoms, indicating that Mo atoms of the $Mo_3(HHTT)_2$ monolayer can act as the active sites. The band structure and density of states of $Mo_3(HHTT)_2$ monolayer were calculated (Fig. S2a-b). It indicated that the $Mo_3(HHTT)_2$ monolayer possess a metal property due to the fermi level crossed the electronic density of states.

The bonding mechanism between the N_2 molecule and $Mo_3(HHTT)_2$ monolayer was further studied. The optimized structure of N_2 adsorption on $Mo_3(HHTT)_2$ monolayer in the end-on configuration is described in Fig. 5(a). The Mo−N length for the N_2 and Mo atom is 1.99 Å, which is smaller than that of the M−O bond of 2.03 Å. The length of N−N bond of N_2 adsorption on $Mo_3(HHTT)_2$ monolayer is elongated to 1.14 Å compared to the isolated N_2 (1.11 Å) molecule. The charge density difference (CDD) was further investigated for N_2 adsorption on $Mo_3(HHTT)_2$ monolayer, as shown in Fig. 5(b). The approximately 0.20*e* per electric charge is transferred to N-N from the Mo-O bond, i.e., the charges of Mo atoms can be transferred to the antibonding orbitals of N_2. Thus, the $Mo_3(HHTT)_2$ monolayer can activate the inert N_2 gas molecules. Fig. 5(c) is the spin density diagram of N_2 adsorption on $Mo_3(HHTT)_2$ monolayer. The total magnetic moment of the N_2 adsorbed on $Mo_3(HHTT)_2$ is 5.55 μB, which is reduced compared to that of $Mo_3(HHTT)_2$ (i.e., 6.94 μB) monolayer. Most of the spin density is distributed around the Mo atom, with the magnetic moment around the N atoms accounting for only a small proportion. These results indicate that the activation source for N≡N is attributed to the contribution of spin density transfer interactions between N and Mo atoms.

To obtain an in-depth understanding of the bonding mechanism of N_2 on $Mo_3(HHTT)_2$ monolayer, the partial density of states (PDOS) for the gas N_2 molecule and the N_2 adsorbed on $Mo_3(HHTT)_2$ monolayer were investigated as shown in Figs. 5(d) and 5(e). Results indicate that the electronic states between the two orbitals--p molecular orbitals of the N atom and d orbitals of the Mo atom have a remarkable overlap in all the energy ranges. The electronic redistribution between Mo atoms and N_2 forms phenomena of splitting and hybridization for the antibonding orbitals of N_2. The 3σ orbitals of N_2 on $Mo_3(HHTT)_2$ monolayer shift the Fermi level relative to that of the free N_2 molecule, which indicates that there are electrons donated to the 4d orbitals of the Mo atom from 2π and 3σ orbitals of N_2. Meanwhile, due to electrons of the occupied orbitals of the Mo atom transferring to the 2π* orbitals of N_2, the 2π* peak

moves towards the Fermi level. The above analysis results explain the mechanisms of the π* back-donation and σ-donation as shown in Fig. 6(a) [46, 69]. Therefore, the N≡N triple bond of N_2 adsorption on the $Mo_3(HHTT)_2$ monolayer in the end-on configuration is weakened via the strong d-2π* coupling.

The σ-donation and π* back-donation mechanisms can often be inferred from the crystal orbital Hamilton population (COHP). Therefore, Fig. 6(b) displays the calculated COHPs of Mo-N and N-N of the N_2 adsorption on the $Mo_3(HHTT)_2$ monolayer. The unoccupied 3σ orbital becomes an antibonding orbital (marked in the red circle in Figure 6(b)) after N_2 adsorption onto the $Mo_3(HHTT)_2$ monolayer, indicating that the lone pair electrons of N_2 are transferred to the Mo atom. Moreover, the occupied 2π* orbital of N_2 is located around the Fermi level, which is marked in the brown circle in Figure 6(b). Results indicate the existence of the d-2π* coupling. The antibonding state of Mo-N is farther from the Fermi level than the N-N antibonding state in the 0 ~ 1.0 eV energy region. Thus, the N-N antibonding orbitals are filled with injected electrons, which are crucial for the catalysis of the $Mo_3(HHTT)_2$ monolayer.

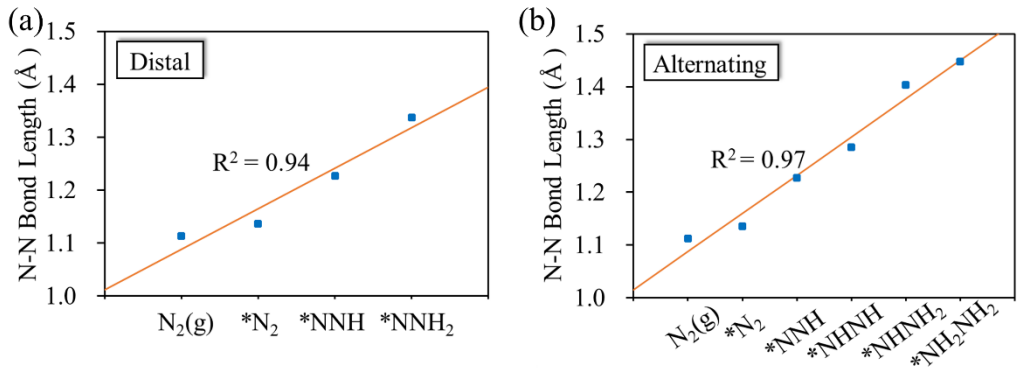

Figure 7. The N-N length of intermediates along the (a) distal and (b) alternating pathways. Calculated details are given in Table S5.

In order to further insight the NRR catalytic properties of the $Mo_3(HHTT)_2$ monolayer, the N−N lengths of each intermediate along the distal and alternating pathways are calculated, and the obtained results are displayed in Figs. 7(a) and 7(b).

The activation process of N_2 molecules on the surface of $Mo_3(HHTT)_2$ monolayer can be traced by the bond length of N−N in the intermediates. The longer the N−N bond of the intermediates is, the greater the amount of activation of the N_2 molecule [70, 71]. The N−N bond length of intermediates is linearly increased for both the distal and alternating pathways with their best determination coefficients of 0.94 and 0.97, respectively. Thus, the N_2 was activated gradually. The $Mo_3(HHTT)_2$ monolayer can fully activate N_2 molecule.

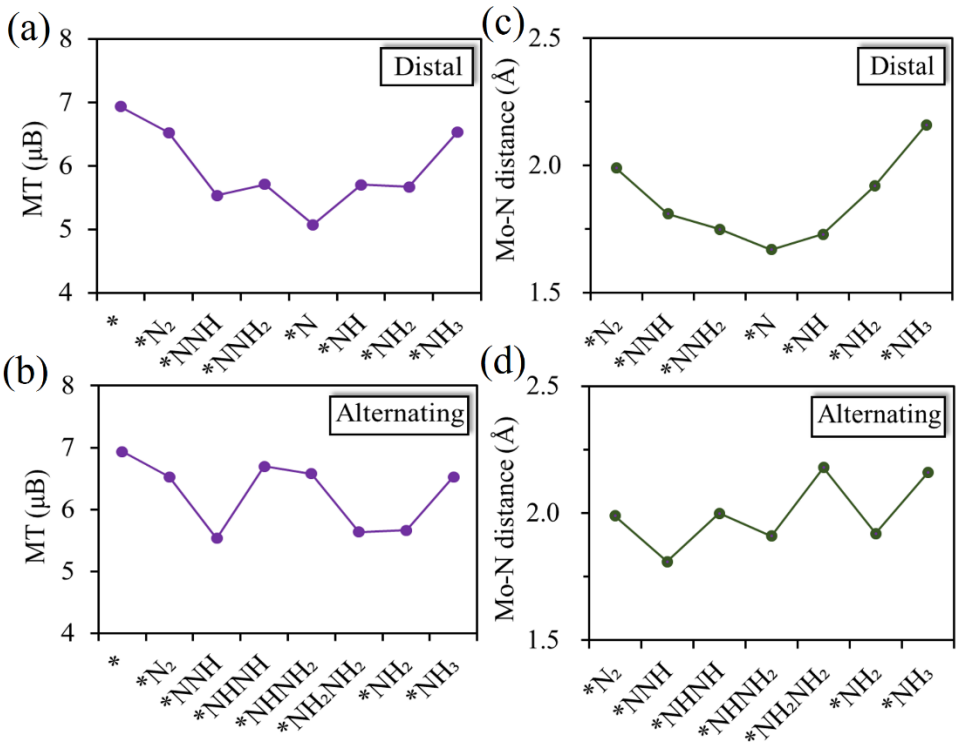

Figure 8. The total magnetic moment of intermediates via (a) distal and (b) alternating pathways. The distances of Mo–N of intermediates via (c) distal and (d) alternating pathways.

The total magnetic moments of intermediates for along distal and alternating pathways were obtained, and the results are shown in Figs. 8(a) and 8(b). The details of values are listed in Table S6. Due to the charge transfer, the total magnetic moments of each intermediate of NRR are decreased to about 5.07-6.70 μB. In the NNR process on the $Mo_3(HHTT)_2$ monolayer, the spin density of the intermediates is mainly from the

Mo atoms, whereas the adsorbed species contribute little to the total density (Fig. S3). The interactions of the spin density between the Mo atoms and the adsorbed species leading to an effective process for NRR [35].

Figs. 8(c) and 8(d) show the distances of the Mo−N bonds of the intermediates along the distal and alternating pathways. For distal pathway, there is a downward trend for the Mo−N distances form *N_2 to *N, which has an inversely proportional relationship with the change length in the N-N bond of intermediates. This variation facilitates the activation of N_2. Moreover, there is an upward trend of intermediates from *N to *NH_3 along the distal pathway. The alternating pathway exhibits a wave-like variation of the length of Mo−N distances, which can be attributed to alternating attacking of proton-electron pairs during the hydrogenation process.

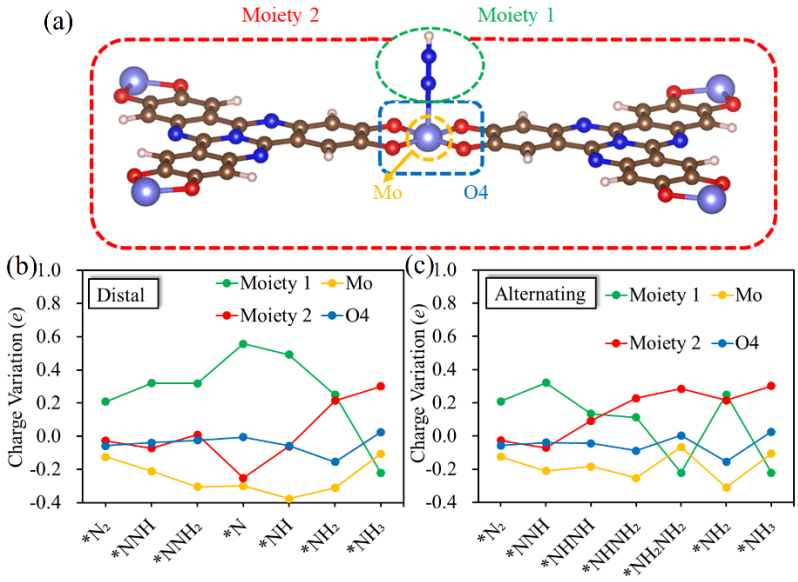

Figure 9. (a) Schematic diagram of four moieties of intermediates for NRR. The diagram of charge variation of these moieties on the $Mo_3(HHTT)_2$ monolayer along the (b) distal and (c) alternating pathways.

The Bader charge transfers of intermediates at each hydrogenation step are evaluated along the distal and alternating pathways. Each hydrogenated system is divided into four moieties, i.e., the moiety 1 (*NxHy), the moiety 2 (HHTT), Mo atom, and O4 unit.

The scheme of four moieties of intermediates is shown in Fig. 9(a). Fig. 9(b) shows the calculated charge variations of the intermediates for all the hydrogenation steps of the $Mo_3(HHTT)_2$ monolayer along distal pathway. For N_2 adsorbed on $Mo_3(HHTT)_2$ monolayer, the N_2 can obtain 0.21*e* mainly from Mo atom. In the following hydrogenation steps, the moiety 1(*NxHy) acts as an electron acceptor until the formation of $*NH_3$. At the same time, the Mo atom acts as the charge emitter and lose electrons in the range of 0.11 ~ 0.38*e*. In the NH_3 formation process, the charge transfers from $*NH_3$ to $Mo_3(HHTT)_2$ monolayer can be clearly observed, which is the reason why NH_3 needs a high desorption energy. For alternating pathway as shown in Fig. 9(c), the moiety 1 gains electrons in the range of 0.11 ~ 0.32*e* until formation of $*NH_2NH_2$. The charge of the $*NH_2NH_2$ are mainly transferred to the moiety 2 (0.28*e*), which indicates that the $Mo_3(HHTT)_2$ monolayer can reasonably regulate the charge transfer in the NRR process. In general, the Mo atom effectively transfers electrons to the intermediates, and could serve as NRR active sites. Moreover, the O4 unit can transport electrons between Mo atom and the organic ligands. Therefore, the cooperative interaction of Mo atom and organic ligands contributes to the catalytic performance of the $Mo_3(HHTT)_2$ monolayer for the NRR.

3.5 Selectivity and stability of the $Mo_3(HHTT)_2$

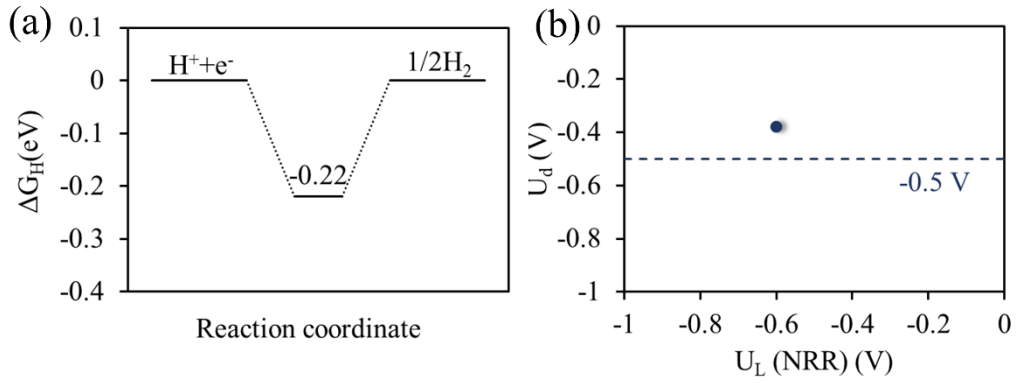

Figure 10. (a) Gibbs free energy for the HER of $Mo_3(HHTT)_2$ monolayer. (b) The diagram of U_L(NRR) versus U_d on the $Mo_3(HHTT)_2$ monolayer of the NRR process.

The blue dashed line indicates the U_d of the metal-based benchmark.

The critical competitive reaction, i.e., HER, of NRR catalytic activity on $Mo_3(HHTT)_2$ monolayer was further considered. The ΔG values of the two hydrogenation steps of the HER on the $Mo_3(HHTT)_2$ monolayer are described in Fig. 10(a). According to the previous study [72], the step of $*H \rightarrow H_2$ is the PDS of the HER. The U_L of the HER on the surface of the $Mo_3(HHTT)_2$ monolayer is −0.22 V. The selectivity of the $Mo_3(HHTT)_2$ monolayer can be measured by the potential difference (U_d) between the U_L of NRR and HER, i.e., $U_d = U_L(NRR) - U_L(HER)$ [73]. The greater the positive value of U_d, the better the selectivity of the NRR on the $Mo_3(HHTT)_2$ monolayer. The value of U_d is more positive than the metal-based benchmark (approximately −0.5 V), as shown in Fig. 10(b) [74, 75], which indicates a higher selectivity for the NRR over the HER. The value of U_d for the $Mo_3(HHTT)_2$ monolayer is -0.38 V, indicating that the $Mo_3(HHTT)_2$ monolayer is the favorite one for the NRR process rather than the HER. The ab initio molecular dynamics (AIMD) simulation was used to evaluate the structural stability of the $Mo_3(HHTT)_2$ monolayer, which was performed at 300 K for 4000 fs. As shown in Fig. S4, the total energy of $Mo_3(HHTT)_2$ monolayer finally oscillates around the initial value as the simulation proceed. Moreover, the surface morphology is almost not changed, and the framework is slightly distorted, indicating that the $Mo_3(HHTT)_2$ monolayer is thermal stable. We believe that the $Mo_3(HHTT)_2$ monolayer is a durable electrocatalyst under reduction process.

4. Conclusions

In summary, a series of 2D c-MOFs, i.e., $TM_3(HHTT)_2$ (TM = Sc, Ti, V, Cr, Mo, W, Mn, Fe, Co, Ni, Cu and Zn) as candidates for the NRR were systematically studied using the DFT computations. The calculated results show that the $Mo_3(HHTT)_2$ monolayer has the best electrocatalytic performance for the NRR process along the distal pathway with a low U_L of -0.60 V. The good stability of the $Mo_3(HHTT)_2$ monolayer is further proven. The dissolution potential and formation energy of the

$Mo_3(HHTT)_2$ monolayer have also been calculated, indicating that the $Mo_3(HHTT)_2$ monolayer have high thermodynamic stability and could be efficiently synthesized experimentally. Moreover, the selectivity of the $Mo_3(HHTT)_2$ monolayer between NRR and HER was studied. The value of U_d for NRR and HER are found to be more positive than the metal-based benchmark (approximately −0.5 V), indicating that the catalytic reaction will proceed in the direction of the NRR rather than HER. Therefore, our study shows that the $Mo_3(HHTT)_2$ monolayer can be used as a highly stable and highly selective electrocatalyst for NRR.

Declaration of Competing Interest:
There are no conflicts to declare.

Acknowledgement:

This work was supported by International Exchange Grant (IEC/NSFC/201078) through the National Natural Science Foundation of China and Royal Society UK.

References:

[1] Service RF. CHEMISTRY New recipe produces ammonia from air, water, and sunlight. Science 2014;345:610-610.
[2] Guo WH, Zhang KX, Liang ZB, Zou RQ, Xu Q. Electrochemical nitrogen fixation and utilization: theories, advanced catalyst materials and system design. Chem Soc Rev 2019;48:5658-716.
[3] van Kessel MAHJ, Speth DR, Albertsen M, Nielsen PH, Op den Camp HJM, Kartal B, et al. Complete nitrification by a single microorganism. Nature 2015;528:555-9.
[4] Kitano M, Inoue Y, Yamazaki Y, Hayashi F, Kanbara S, Matsuishi S, et al. Ammonia synthesis using a stable electride as an electron donor and reversible hydrogen store. Nat Chem 2012;4:934-40.
[5] Suryanto BHR, Du HL, Wang DB, Chen J, Simonov AN, MacFarlane DR. Challenges and prospects in the catalysis of electroreduction of nitrogen to ammonia. Nat Catal 2019;2:290-6.
[6] van der Ham CJM, Koper MTM, Hetterscheid DGH. Challenges in reduction of dinitrogen by proton and electron transfer. Chem Soc Rev 2014;43:5183-91.
[7] Lv C, Qian YM, Yan CS, Ding Y, Liu YY, Chen G, et al. Defect Engineering Metal-Free Polymeric Carbon Nitride Electrocatalyst for Effective Nitrogen Fixation under Ambient Conditions. Angew Chem Int Ed 2018;57:10246-50.
[8] Martin AJ, Shinagawa T, Perez-Ramirez J. Electrocatalytic Reduction of Nitrogen: From Haber-Bosch to Ammonia Artificial Leaf. Chem 2019;5:263-83.
[9] Qing G, Ghazfar R, Jackowski ST, Habibzadeh F, Ashtiani MM, Chen CP, et al. Recent Advances and Challenges of Electrocatalytic N-2 Reduction to Ammonia. Chem Rev 2020;120:5437-516.
[10] Tang C, Qiao SZ. How to explore ambient electrocatalytic nitrogen reduction reliably and insightfully. Chem Soc Rev 2019;48:3166-80.
[11] Yao DZ, Tang C, Li LQ, Xia BQ, Vasileff A, Jin HY, et al. In Situ Fragmented Bismuth Nanoparticles for Electrocatalytic Nitrogen Reduction. Adv Energy Mater 2020;10:2001289.
[12] Wang SY, Ichihara F, Pang H, Chen H, Ye JH. Nitrogen Fixation Reaction Derived from Nanostructured Catalytic Materials. Adv Funct Mater 2018;28:1803309.
[13] Quan CY, Xiao SS, Yi YW, Sun DZ, Ji SL, Zhou S, et al. Explore the underlying mechanism of graphitic C3N5-hosted single-atom catalyst for electrocatalytic nitrogen fixation. Inter J Hydrogen Energ 2022;47:22035-44.
[14] Xu L, Yang LM, Ganz E. Electrocatalytic Reduction of N-2 Using Metal-Doped Borophene. ACS Appl Mater Interfaces 2021;13:14091-101.
[15] Choi C, Back S, Kim NY, Lim J, Kim YH, Jung Y. Suppression of Hydrogen Evolution Reaction in Electrochemical N-2 Reduction Using Single-Atom Catalysts: A Computational Guideline. ACS Catal 2018;8:7517-25.
[16] Wang R, He CZ, Chen WX, Fu L, Zhao CX, Huo JR, et al. Design strategies of two-dimensional metal-organic frameworks toward efficient electrocatalysts for N-2 reduction: cooperativity of transition metals and organic linkers. Nanoscale 2021;13:19247-54.

[17] He HM, Zhu QQ, Yan Y, Zhang HW, Han ZY, Sun HM, et al. Metal-organic framework supported Au nanoparticles with organosilicone coating for high-efficiency electrocatalytic N2 reduction to NH3. Appl Catal B-Environ 2022;302:120840.
[18] Li LS, Martirez JMP, Carter EA. Prediction of Highly Selective Electrocatalytic Nitrogen Reduction at Low Overpotential on a Mo-Doped g-GaN Monolayer. ACS Catal 2020;10:12841-57.
[19] Liu J, Liang TX, Wang F, Lai WS, Liu YJ. Enhancing of nitrogen reduction reaction to ammonia through CoB4-embedded graphene: Theoretical investigation. Inter J Hydrogen Energ 2020;45:9555-63.
[20] Liang Z, Liu C, Chen MW, Luo MM, Qi XP, Peera SG, et al. Theoretical screening of di-metal atom (M = Fe, Co, Ni, Cu, Zn) electrocatalysts for ammonia synthesis. Inter J Hydrogen Energ 2020;45:31881-91.
[21] Zhang YZ, Hu J, Zhang CX, Cheung ATF, Zhang Y, Liu LF, et al. Mo2C embedded on nitrogen-doped carbon toward electrocatalytic nitrogen reduction to ammonia under ambient conditions. Inter J Hydrogen Energ 2021;46:13011-9.
[22] Li J, Yin HM, Li XB, Okunishi E, Shen YL, He J, et al. Surface evolution of a Pt-Pd-Au electrocatalyst for stable oxygen reduction. Nat Energy 2017;2:17111.
[23] Wang DB, Azofra LM, Harb M, Cavallo L, Zhang XY, Suryanto BHR, et al. Energy-Efficient Nitrogen Reduction to Ammonia at Low Overpotential in Aqueous Electrolyte under Ambient Conditions. ChemSusChem 2018;11:3416-22.
[24] Nazemi M, Panikkanvalappil SR, El-Sayed MA. Enhancing the rate of electrochemical nitrogen reduction reaction for ammonia synthesis under ambient conditions using hollow gold nanocages. Nano Energy 2018;49:316-23.
[25] Liu CW, Li QY, Zhang J, Jin YG, MacFarlane DR, Sun CH. Conversion of dinitrogen to ammonia on Ru atoms supported on boron sheets: a DFT study. J Mater Chem A 2019;7:4771-6.
[26] Ji S, Wang ZX, Zhao JX. A boron-interstitial doped C2N layer as a metal-free electrocatalyst for N-2 fixation: a computational study. J Mater Chem A 2019;7:2392-9.
[27] Liu SQ, Liu YW, Gao XP, Tan YJ, Cheng ZW, Shen ZM, et al. Two-Dimensional Transition Metal Porphyrin Sheets as a Promising Single-Atom-Catalyst for Dinitrogen Electrochemical Reduction to Ammonia: A Theoretical Study. J Phys Chem C 2020;124:1492-9.
[28] Tan JB, He XB, Yin FX, Liang X, Li GR. Post-synthetic Ti exchanged UiO-66-NH2 metal-organic frameworks with high faradaic efficiency for electrochemical nitrogen reduction reaction. Inter J Hydrogen Energ 2021;46:31647-58.
[29] Li TS, Xia JJ, Xian HH, Chen QR, Xu K, Gu Y, et al. Fe(III) grafted MoO3 nanorods for effective electrocatalytic fixation of atmospheric N-2 to NH3. Inter J Hydrogen Energ 2022;47:3550-5.
[30] Ali S, Olanrele S, Liu TF, Lian Z, Si CW, Yang M, et al. Single Au Anion Can Catalyze Acetylene Hydrochlorination: Tunable Catalytic Performance from Rational Doping. J Phys Chem C 2019;123:29203-8.

[31] Yang XF, Wang AQ, Qiao BT, Li J, Liu JY, Zhang T. Single-Atom Catalysts: A New Frontier in Heterogeneous Catalysis. Acc Chem Res 2013;46:1740-8.
[32] Zhao WH, Zhang LF, Luo QQ, Hu ZP, Zhang WH, Smith S, et al. Single Mo-1(Cr-1) Atom on Nitrogen-Doped Graphene Enables Highly Selective Electroreduction of Nitrogen into Ammonia. ACS Catal 2019;9:3419-25.
[33] Wang C, Guo C. Screening of transition metal single atom catalysts supported on B-36 cluster for nitrogen fixation. Inter J Hydrogen Energ 2022;47:5281-91.
[34] Chen YB, Zhang XY, Qin JQ, Liu RP. Theoretical screening of highly efficient single-atom catalysts for nitrogen reduction based on a defective C3N monolayer. Inter J Hydrogen Energ 2022;47:5292-306.
[35] Li XF, Li QK, Cheng J, Liu LL, Yan Q, Wu YC, et al. Conversion of Dinitrogen to Ammonia by FeN3-Embedded Graphene. J Am Chem Soc 2016;138:8706-9.
[36] Huang Y, Yang TT, Yang L, Liu R, Zhang GZ, Jiang J, et al. Graphene-boron nitride hybrid-supported single Mo atom electrocatalysts for efficient nitrogen reduction reaction. J Mater Chem A 2019;7:15173-80.
[37] Liu JJ, Yang D, Zhou Y, Zhang G, Xing GL, Liu YP, et al. Tricycloquinazoline-Based 2D Conductive Metal-Organic Frameworks as Promising Electrocatalysts for CO2 Reduction. Angew Chem Int Ed 2021;60:14473-9.
[38] Liu JJ, Song XY, Zhang T, Liu SY, Wen HR, Chen L. 2D Conductive Metal-Organic Frameworks: An Emerging Platform for Electrochemical Energy Storage. Angew Chem Int Ed 2021;60:5612-24.
[39] Calbo J, Golomb MJ, Walsh A. Redox-active metal-organic frameworks for energy conversion and storage. J Mater Chem A 2019;7:16571-97.
[40] Li C, Zhang LL, Chen JQ, Li XL, Sun JW, Zhu JW, et al. Recent development and applications of electrical conductive MOFs. Nanoscale 2021;13:485-509.
[41] Xue YP, Zhao GC, Yang RY, Chu F, Chen J, Wang L, et al. 2D metal-organic framework-based materials for electrocatalytic, photocatalytic and thermocatalytic applications. Nanoscale 2021;13:3911-36.
[42] Xu XJ, Yang XJ, Hou XL, Xiao BB, Mi JL. Nitrogen electroreduction on two-dimensional pi-conjugated metal bis (dithiolene) complex nanosheets: A density functional theory study. Catal Commun 2020;138:105863.
[43] Li BS, Du WH, Wu Q, Dai Y, Huang BB, Ma YD. Coronene-Based 2D Metal-Organic Frameworks: A New Family of Promising Single-Atom Catalysts for Nitrogen Reduction Reaction. J Phys Chem C 2021;125:20870-6.
[44] Feng Z, Yang ZL, Meng XW, Li FC, Guo ZY, Zheng S, et al. Two-dimensional metal-organic framework Mo-3(C2O)(12) as a promising single-atom catalyst for selective nitrogen-to-ammonia conversion. J Mater Chem A 2022;10:4731-8.
[45] Zhang J, Zhu XY, Geng WX, Li TC, Li MM, Fang CB, et al. Mo-3(C6X6)(2) (X = NH,S,O) monolayers: two-dimensional conductive metal-organic frameworks as effective electrocatalysts for the nitrogen reduction reaction. J Energy Chem 2021;61:71-6.
[46] Lv XS, Wei W, Wang H, Li FP, Huang BB, Dai Y, et al. Nitrogen-free TMS4-

centers in metal-organic frameworks for ammonia synthesis. J Mater Chem A 2020;8:20047-53.
[47] Dou JH, Arguilla MQ, Luo Y, Li J, Zhang WZ, Sun L, et al. Atomically precise single-crystal structures of electrically conducting 2D metal-organic frameworks. Nat Mater 2021;20:222-8.
[48] Chen X, Luo L, Ge F. Two-Dimensional Metal-Organic Frameworks as Ultrahigh-Performance Electrocatalysts for the Fuel Cell Cathode: A First-Principles Study. Langmuir 2022;38:4996-5005.
[49] Kresse G, Furthmuller J. Efficient iterative schemes for ab initio total-energy calculations using a plane-wave basis set. Phys Rev B 1996;54:11169-86.
[50] Perdew JP, Chevary JA, Vosko SH, Jackson KA, Pederson MR, Singh DJ, et al. Atoms, Molecules, Solids, and Surfaces - Applications of the Generalized Gradient Approximation for Exchange and Correlation. Phys Rev B 1992;46:6671-87.
[51] Perdew JP, Burke K, Ernzerhof M. Generalized gradient approximation made simple. Phys Rev Lett 1996;77:3865-8.
[52] Blochl PE. Projector Augmented-Wave Method. Phys Rev B 1994;50:17953-79.
[53] Grimme S, Antony J, Ehrlich S, Krieg H. A consistent and accurate ab initio parametrization of density functional dispersion correction (DFT-D) for the 94 elements H-Pu. J Chem Phys 2010;132:154104.
[54] Evarestov RA, Smirnov VP. Modification of the Monkhorst-Pack special points meshes in the Brillouin zone for density functional theory and Hartree-Fock calculations. Phys Rev B 2004;70:233101.
[55] Wang V, Xu N, Liu JC, Tang G, Geng WT. VASPKIT: A user-friendly interface facilitating high-throughput computing and analysis using VASP code. Comput Phys Commun 2021;267:108033.
[56] Norskov JK, Rossmeisl J, Logadottir A, Lindqvist L, Kitchin JR, Bligaard T, et al. Origin of the overpotential for oxygen reduction at a fuel-cell cathode. J Phys Chem B 2004;108:17886-92.
[57] Rossmeisl J, Logadottir A, Norskov JK. Electrolysis of water on (oxidized) metal surfaces. Chem Phys 2005;319:178-84.
[58] Johnson RD. NIST Computational chemistry comparison and benchmark database. Abstr Papers Am Chem Soc 2005;230:U1015.
[59] Greeley J, Norskov JK. Electrochemical dissolution of surface alloys in acids: Thermodynamic trends from first-principles calculations. Electrochim Acta 2007;52:5829-36.
[60] Guo XY, Gu JX, Lin SR, Zhang SL, Chen ZF, Huang SP. Tackling the Activity and Selectivity Challenges of Electrocatalysts toward the Nitrogen Reduction Reaction via Atomically Dispersed Biatom Catalysts. J Am Chem Soc 2020;142:5709-21.
[61] Long J, Fu XY, Xiao JP. The rational design of single-atom catalysts for electrochemical ammonia synthesis via a descriptor-based approach. J Mater Chem A 2020;8:17078-88.
[62] Wang SH, Wei W, Lv XS, Huang BB, Dai Y. W supported on g-CN manifests high

activity and selectivity for N-2 electroreduction to NH3. J Mater Chem A 2020;8:1378-85.
[63] Castellano-Varona B, Harb M, Arana J, Cavallo L, Azofra LM. In silico design of novel NRR electrocatalysts: cobalt-molybdenum alloys. Chem Commun 2020;56:13343-6.
[64] Skulason E, Bligaard T, Gudmundsdottir S, Studt F, Rossmeisl J, Abild-Pedersen F, et al. A theoretical evaluation of possible transition metal electro-catalysts for N-2 reduction. Phys Chem Chem Phys 2012;14:1235-45.
[65] Anderson JS, Rittle J, Peters JC. Catalytic conversion of nitrogen to ammonia by an iron model complex. Nature 2013;501:84-7.
[66] Fang C, An W. Single-metal-atom site with high-spin state embedded in defective BN nanosheet promotes electrocatalytic nitrogen reduction. Nano Res 2021;14:4211-9.
[67] Zhao JX, Chen ZF. Single Mo Atom Supported on Defective Boron Nitride Monolayer as an Efficient Electrocatalyst for Nitrogen Fixation: A Computational Study. J Am Chem Soc 2017;139:12480-7.
[68] Lin YC, Teng PY, Chiu PW, Suenaga K. Exploring the Single Atom Spin State by Electron Spectroscopy. Phys Rev Lett 2015;115: 206803.
[69] Zhang J, Zhao YM, Wang Z, Yang G, Tian JL, Ma DW, et al. Boron-decorated C9N4 monolayers as promising metal-free catalysts for electrocatalytic nitrogen reduction reaction: a first-principles study. New J Chem 2020;44:422-7.
[70] Huang CX, Li GL, Yang LM, Ganz E. Ammonia Synthesis Using Single-Atom Catalysts Based on Two- Dimensional Organometallic Metal Phthalocyanine Monolayers under Ambient Conditions. Acs Appl Mater Inter 2021;13:608-21.
[71] Wen L, Ren CJ, Zou Y, Lin W, Ding KN. Why it is S-rich around Mo atom in the nitrogenase: A DFT investigation. Appl Surf Sci 2020;534:147595.
[72] Singh AR, Rohr BA, Schwalbe JA, Cargnello M, Chan K, Jaramillo TF, et al. Electrochemical Ammonia Synthesis-The Selectivity Challenge. ACS Catal 2017;7:706-9.
[73] Hu XM, Guo SY, Zhang SL, Guo XY, Li YF, Huang SP, et al. Two-dimensional transition metal diborides: promising Dirac electrocatalysts with large reaction regions toward efficient N-2 fixation. J Mater Chem A 2019;7:25887-93.
[74] Chen Z, Zhao JX, Cabrera CR, Chen ZF. Computational Screening of Efficient Single-Atom Catalysts Based on Graphitic Carbon Nitride (g-C3N4) for Nitrogen Electroreduction. Small Methods 2019;3:1800368.
[75] Montoya JH, Tsai C, Vojvodic A, Norskov JK. The Challenge of Electrochemical Ammonia Synthesis: A New Perspective on the Role of Nitrogen Scaling Relations. ChemSusChem 2015;8:2180-6.